Soft Matter

PAPER

View Article Online
View Journal

Cite this: DOI: 10.1039/d5sm01104c

Propulsion of laser printed polymer micro-rods by a low frequency electric field in nematic liquid crystals

Linsy Jane Selvin Robert, [a] Ashish Chandra Das, [ce] Vida Jurečič, [a] Vid Bobnar, [ad] Oleg D. Lavrentovich, [bce] Miha Ravnik [af] and Igor Muševič *[af]

Received 4th November 2025,
Accepted 27th January 2026

DOI: 10.1039/d5sm01104c

rsc.li/soft-matter-journal

We use polarized optical microscopy and confocal fluorescence microscopy to explore electric-field induced swimming of direct laser written polymer microrods in a nematic liquid crystal in the regime of very low frequencies. The rods are of variable aspect ratio and swim in a liquid crystal layer with a thickness comparable to that of the longest rods. We observe significant spatial reorientation of the microrods under an applied electric field, which is characterized by their up and down movement along the applied electric field, oscillation in their tilting with respect to the field, sidewise wobbling of their center of mass and propulsion along the direction perpendicular to the electric field. The velocity of propulsion shows a power law behaviour on the electric field magnitude, $v_x \propto E^{\alpha}$, where α is between 3 and 5 for different aspect ratio rods and can be partially explained by the shear thinning of the viscosity at higher velocity. The time analysis of 3D trajectories of swimming microrods shows a linear coupling of the microrod's center of mass to the applied electric field, and quadratic (*i.e.* dielectric) coupling of the microrod's tilt to the field, which appears to be the main driving mechanism for microrod propulsion.

1 Introduction

Artificial microswimmers have attracted significant interest for their collective behaviour,[1,2] self-assembly,[3,4] and various microswimming propulsion mechanisms.[5] These artificial microswimmers are typically colloidal particles that are propelled by driving them out of equilibrium either by local conversion of energy (chemical, thermal field gradients) or by external fields (electric, magnetic fields, light, or thermal).[6–8]

In the case of colloidal propulsion driven by electric fields, the motion is typically mediated by electro-osmosis, where the applied field induces charge separation and fluid flow around the colloid.[9] The symmetry breaking of the electro-osmotic flow around the colloid is required to have a net propulsion,[10] where the fore-aft asymmetry of the fluid momentum change generates the force, which drives the particle in motion. This can be introduced either by making the colloid anisotropic or by the anisotropy of the medium itself.[11] In the case of isotropic medium, the symmetry breaking is introduced by either the geometry of the particle or the material properties of the colloid. For example, a Janus colloid is typically made by covering one part of the particle. *e.g.* a microsphere, with some additional material, such as a metal.[11] In the case of anisotropic medium, such as nematic liquid crystals (LC), the symmetry breaking is introduced by the director distortions caused by the topological defect type of the colloid and the anisotropic properties of the LC.[12] In such a case, a spherically symmetric colloid made out of a single material can be transported in the LC.

A colloidal particle immersed in a planar-aligned nematic LC interacts with the surrounding LC primarily due to surface anchoring of LC molecules on the colloidal surface. Because the surface of the colloidal particle is a closed surface and because the LC is aligned along that closed surface, topological defects must be created according to the Gauss–Bonnet theorem, to compensate for the topological charge of the particle.[13,14] For example, perpendicular (homeotropic) surface anchoring onto the colloidal particles that have no holes results in the formation of either a −1 hyperbolic hedgehog (point defect) or −1/2 disclination Saturn ring defect in the LC, which have dipolar and quadrupolar symmetry respectively.[15] In case the closed

[a] Condensed Matter Physics Department, Jožef Stefan Institute, Jamova cesta 39, 1000 Ljubljana, Slovenia. E-mail: igor.musevic@ijs.si
[b] Department of Physics, Kent State University, Kent, OH, 44242, USA
[c] Materials Science Graduate Program, Kent State University, Kent, OH, 44242, USA
[d] Jožef Stefan International Postgraduate School, Jamova cesta 39, SI-1000 Ljubljana, Slovenia
[e] Advanced Materials and Liquid Crystal Institute, Kent State University, Kent, OH, 44242, USA
[f] Faculty of Mathematics and Physics, University of Ljubljana, Jadranska 19, 1000 Ljubljana, Slovenia

surface imposes parallel surface anchoring, two surface boojums are created, which makes the colloidal particle and the director distortion around it possess quadrupolar symmetry. This means that the fore-aft symmetry of the director field is broken only in the case of the dipolar nematic colloids, where the colloidal particles are accompanied by a single −1 hyperbolic hedgehog defect. Together with the virtual +1 defect residing in the center of the colloidal particle, they form an elastic (sometimes also called topological) dipole that is collinear with the far field nematic director and points from the hyperbolic hedgehog to the center of the particle.[16] This elastic dipole is the signature of the broken fore–aft symmetry of the system.

Ions are always present in LCs due to chemical decomposition of the material by a DC electric field or diffusion of free charges from the alignment layers or surrounding. Due to the spontaneous dissociation of molecules at the particle–LC interface, the colloidal particles in LCs may also be electrically charged. The dissociated ions, also called the counter-ions, form the diffuse electric double layer with a thickness of the order of Debye screening length.[16] An electric field that is applied to the LC exerts an electric force on charges, separates them and causes their flow along the director field according to the LC anisotropy of electric conductivity.[12] This leads to the LC enabled electro-osmotic flow, which is the key ingredient in driving the colloid out of equilibrium.[12] The electro-osmotic flow in LCs depends on the conductivity anisotropy and the director distortion around the colloid, which is mainly determined by the topological defect.[12] An asymmetric fore–aft flow around the colloid leads to net propulsion along the director.[12] The mechanism of propulsion is also strongly dependent on the properties such as electric conductivity and dielectric permittivity of the LCs.[11] Additionally, surface anchoring, colloidal geometry, and material properties of colloid can also contribute to fore–aft flow asymmetry.[11] Propulsion of spontaneously charged colloids under a direct current (DC) electric field in an anisotropic electrolyte is governed by the balance of the electrostatic pulling force on electric charges and viscous drag force that are for small velocities both proportional to the velocity of the particle, following Smoluchowski's formula $v = \mu E$. Here, the velocity of the particle is collinear with the electric field. For stronger DC fields, velocity (v) of the colloid is a combination of linear and cubic dependence on applied electric field (E), where μ is the electrophoretic mobility and $\mu^{(3)}$ is the field-independent coefficient[17,18] $v = \mu E + \mu^{(3)}E^3$.

The application of a DC electric field to propel colloids in the LC is impractical, as it causes electrochemical decomposition of the LC on the time scale of seconds. Therefore, mechanisms that propel colloidal particles in liquids under an alternating current (AC) electric field are of particular interest. It was shown in the experiments by Gangwal *et al.*[19] that Janus microparticles with one dielectric and one metal coated hemisphere in aqueous suspensions move in a direction that is perpendicular to the applied electric field and the velocity of the particles is proportional to the square of the applied electric field. This was in agreement with the theory of induced-charge electrophoretic propulsion (ICEP),[10,20,21] where the external electric field first polarizes the medium by displacing the charges and the electric field of displaced charges generates the flow of ions in the liquid, resulting in the net propulsion force acting on the particle. While in the experiments by Gangwal *et al.* the fore–aft symmetry is broken by the Janus nature of the particles, Lavrentovich *et al.*[16] have demonstrated that spherically symmetric particles in a nematic LC can also be propelled by the induced-charge electroosmosis of ions dispersed in the LCs. Here, the fore–aft symmetry is broken by the presence of the hyperbolic topological defect, which accompanies the particle and forms an elastic dipole in combination with the particle. In this case the anisotropy of the colloidal geometry, conductivity and the dielectric properties of LCs play an important role in the propulsion mechanics.[18] The LC enabled electrophoretic (LCEEP) motion is complex, and the velocity of the colloidal particle can be parallel, antiparallel or perpendicular to E_z in a homogeneously aligned nematic LC. The velocity (v_x) of the colloid has a quadratic dependence on the electric field applied E_z, with the nematic director $\hat{n}_0 \approx (1, 0, 0)$[16,18] and the relationship between v_x and E_z is:[12]

$$v_x = b\frac{\epsilon_0\bar{\epsilon}}{\eta_{\text{eff}}}\left(\frac{\Delta\sigma}{\bar{\sigma}} - \frac{\Delta\epsilon}{\bar{\epsilon}}\right)RE_z^2$$

Here $\bar{\sigma}$ and $\bar{\epsilon}$ are the average conductivity and dielectric permittivity respectively, and ($\Delta\epsilon$) and ($\Delta\sigma$) are the anisotropies of dielectric constant and conductivity respectively. η_{eff} is the effective viscosity of the nematic, b is a constant and R is the radius of the colloid. Recently, Rajabi *et al.* reported a higher power-law relationship between E_z and v_x, which is also part of LCEEP.[22] The higher order relationship is attributed to the shear-thinning effect of the nematic liquid crystal which can be observed in both very high and very small electric fields.[22] The shear-thinning effect is a non-Newtonian response of the liquid, caused by the motion of the colloid under the electric field causing a shear flow of the nematic LC around it.[22] This influences the effective viscosity, which decreases due to the direction realignment caused by the colloidal motion.[22] Frequency of the AC field also has a strong influence on the velocity of the colloid. Although there have been reports on the frequency dependence of colloidal propulsion velocity in LCs[16,18,23–26] only very few studies have been done at relatively low frequencies (1–20 Hz) in detail. Typically for such experiments complex waveforms with frequency modulation have been used.[27,28] At low driving frequencies, director reorientation around the propelled particle becomes visible and important for the propulsion mechanism.

In terms of topology, microrods are equivalent to microspheres, because both are characterized by zero genus $g = 0$.[29] This results in the same type of hyperbolic hedgehog defect and Saturn ring defect in microrods with homeotropic surface anchoring in nematic LC.[15,30] The preference for the location of the topological defect is a bit different here due to the inherent shape anisotropy of the microrod.[29,30] Research on microrod propulsion in nematic LC remains limited.[31] Rasi *et al.*[31] reported the LCEEP propulsion of micro and nanorods

in nematic LCs along with the observation of microrod constant tilt at a relatively high frequency of 50 Hz. Propulsion of colloids in nematic LCs that have shapes other than spheres or rods remains largely unexplored, with few exceptions.[26] The reason is in the rather limited variety of shapes of colloidal particles that can be chemically synthesized.[32] On the other hand, 2-photon polymerization laser printing (also termed Direct Laser Writing, DLW) has recently emerged as an alternative method that can produce a reasonable quantity of nearly arbitrary shaped colloidal particles of 1–10 μm dimensions. Interactions of DLW printed cone-shaped[33] and bent rods,[34] as well as catalytically propelled DLW printed microswimmers[35] were recently studied in aqueous solutions. DLW printed colloids were also studied in nematic LCs, and Martinez *et al.* reported mutually tangled colloidal knots on 3D printed knotted colloidal particles.[36] Hashemi *et al.*[37] studied topological defects in fractal-shaped colloids with genus $g = 1$. Yuan *et al.*[38] studied pair interactions of DLW printed microhelices in nematic LCs, Nikkhou *et al.*[39] studied topological defects of grooved microrods and microhelices in a nematic LC. While there has been substantial work on topological properties and pair interactions of DLW printed colloids of various shapes in nematic LCs, there is lack of investigation on the swimming properties of DLW printed colloids in nematic LCs.

The aim of this work is to explore electric-field induced swimming of DLW printed polymer rods of variable aspect ratios in the regime of very low frequencies of the driving field that has not been explored before. In this regime, significant spatial reorientation of microrods can be observed, which clearly influences the particle propulsion due to director reorientation and LC flow effects. We 3D print polymer microrods of different aspect ratios to have precise control over their dimensions. We use optical polarized microscopy and 3D real-time fluorescent confocal imaging to systematically investigate the complex propulsion dynamics of active microrods and their 3D trajectories. We observe that all aspect ratio microrods show a threshold of $\sim$0.1 V μm^{-1} for their propulsion. The velocity of propulsion shows a power law behaviour on the electric field magnitude, $v_x \sim E_z^{\alpha}$, where α is between 3 and 5 for different aspect ratio rods, similar to the results of Rajabi *et al.*[22]

Using real-time confocal fluorescent microscopy, we observe three-dimensional trajectories of microrod propulsion in nematic LC under very low frequency of the driving electric field. They are characterized by dynamic tilting of microrods and movement of their centers of mass towards and away from the confining surfaces in response to applied electric fields. This results in helical-like motion of the rod's center of mass. This helical-like motion of the center of mass of the microrods, combined with synchronized oscillations of the tilting angle of the microrods results in time-periodic colour changes of the surroundings of the microrods when imaged with red-plate polarized microscopy.

This work is divided into two experimental sections. In the first part, we explore the electric field dependence of microrods' velocity at low frequencies of 6 Hz and 11 Hz, respectively. In the second part, we present a 3D fluorescent confocal imaging study of propulsion dynamics of microrods at ultra-low frequency, which clearly shows the three dimensional, helical-like trajectory of the active microrods.

2 Materials and methods

2.1 Sample preparation

We used MLC-6608 (purchased from Merck), a nematic liquid crystal (LC) with negative dielectric anisotropy, very low birefringence $\Delta n = 0.08$[31] and a positive conductivity anisotropy for all our experiments. To check the actual purity of the LC in measuring cells, the dielectric and conductive anisotropy were measured for the liquid crystal in the interval 0.01 Hz to 1 MHz (refer Fig. S1 and S2 in the SI). The dielectric anisotropy of the LC in cells is negative in this frequency range, at 1 Hz the values are $\Delta\varepsilon = -1.84$ ($\varepsilon_{\parallel} = 5.77$ and $\varepsilon_{\perp} = 7.61$), and at 10 Hz the values are $\Delta\varepsilon = -2.91$ ($\varepsilon_{\parallel} = 4.07$ and $\varepsilon_{\perp} = 6.98$), in agreement with reported literature values. The measured anisotropy of the conductivity is positive, and slightly increases with frequency up to 1 kHz (see the SI). The measured conductivity is also very much dependent on the sample used and could vary for $\sim$2 orders of magnitude, depending on sample preparation, as presented in the SI (refer to Fig. S2 in the SI). In the frequency interval from 1 to 100 Hz, for all samples the anisotropy of conductivity is positive, $\Delta\sigma \sim 7.9 \times 10^{-10}$ S m^{-1} in agreement with literature reports.[24,43]

Planar cells were used for the measurements of electric field propulsion of DLW printed polymer microrods. Two indium tin oxide-coated glasses of thickness 0.7 mm (produced by Colorado Concept Coatings LLC) were spin-coated with low-pretilt polyimide (Nissan PI-5291) and rubbed with a velvet cloth to induce good planar alignment for the LC molecules. The glasses were sandwiched in a way that both rubbing directions were parallel to each other and were glued by UV curing 9 μm diameter Melamine microspheres (produced by Nippon Shokubai) mixed with UV curable glue for a well-defined cell thickness. Wires were attached to the ITO electrodes using a two-component silver paste (EPO-TEK H20E) and were cured at 110 °C for 20 minutes.

The colloids here were 3D printed using the two-photon polymerization technique with a Photonic Professional GT2 system (Nanoscribe GmbH, Germany) on an ITO (70–100 Ohms sq^{-1}) coated coverslip (producer: diamond coatings Ltd; 22 mm × 22 mm, no. 1.5). A 63× objective (Zeiss, 1.4 NA Oil Dic, Plan Apochromat) was used for printing, which has a printing area of 100 μm × 100 μm. Details of the CAD design of rods and printing procedure are described in the SI (refer to Fig. S3 in the SI). Arrays of polymer microrods of different aspect ratios (Table 1) were printed on a glass and ITO-coated coverslips using negative photoresist IP-Dip commercially purchased from the producer (Nanoscribe GmbH) with dip-in liquid lithography mode. In this mode of printing, the glass is above the objective, and the space between the glass surface and the objective lens is filled with the resin (Fig. 1(b)). The printing starts at the resin–glass interface and proceeds downwards, which means

Table 1 Dimensions, aspect ratios, and photoresists used for microrods

Dimension of microrod	Aspect ratio (length/diameter)	Photoresist
Length = 5 μm; diameter = 2 μm	2.5	IP-Dip
Length = 10 μm; diameter = 2 μm	5	IP-Dip
Length = 15 μm; diameter = 2 μm	7.5	IP-Dip

that the printing laser beam always passes through the non-polymerized resin, which minimizes possible aberrations and scattering of the printing beam on already polymerized parts of the object.

The structures were initially developed with propylene glycol monomethyl ether acetate (Sigma Aldrich) for 20 minutes and then with isopropyl alcohol for 10 minutes. To induce homeotropic surface anchoring on the microrods, the colloids were initially exposed to UVO plasma for 5 minutes, then immersed in 2 v/v% aqueous dimethyloctadecyl[3-(trimethoxysilylpropyl)]-ammonium chloride solution (Sigma Aldrich) for 5 minutes while gently swirling in a clockwise direction to have a flow of the solution around the microrods. The sample was thoroughly washed with running water for 10 minutes and then with deionized water to remove the excess silane and baked at 110 °C for 1 hour inside a closed oven. 0.2–1 μL of LC was drop cast on the printed microrods, and the microrods were detached from the surface of the substrate by knocking them loose at its base using pulled glass capillary needles attached to a microinjector (Eppendorf FemtoMan). The tip inner diameter varied from 40 μm to 60 μm. The colloidal LC mixture was simultaneously collected into the capillary tip by capillary forces, which was later filled into a planar cell by capillary forces. More LC was drop-cast to collect the residual particles with the capillary needle. The cells were filled with the colloid–LC mixture by capillary action from the capillary needle.

To image the microrods under a fluorescent confocal microscope (FCM), a 0.4% concentration of Pyrromethene-580 dye (produced by Sigma Aldrich) with MLC-6608 liquid crystals was used for fluorescence. The dye molecules align parallel to the liquid crystal molecules. To have a homogeneous mixture of dye in liquid crystals, the dye was initially dissolved in acetone which was then mixed with LC in a vortex stirrer. Later, it was kept inside a closed oven overnight at 60 °C to evaporate the residual acetone.

2.2 Optical microscopy, viscosity measurement, fluorescent confocal imaging and data analysis

Square waveform of alternating current (AC) electric fields was applied normal to the cell surface by using a function generator (HAMEG HMF2525). The voltage signals were monitored by a two-channel oscilloscope. The propulsion of microrods in the

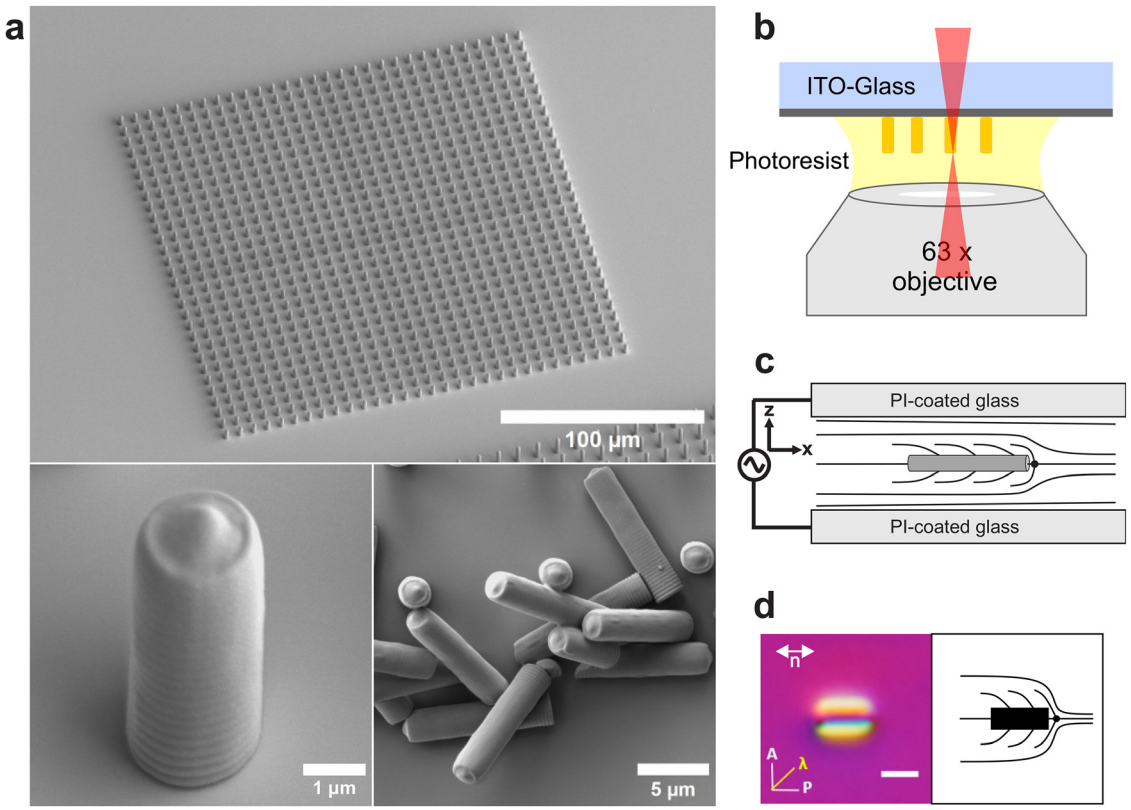

Fig. 1 (a) Scanning electron microscopy (SEM) images of an array of 30 × 30 3D-printed microrods (length = 5 μm, diameter = 2 μm), a zoomed-in standing microrod, and fallen microrods (length = 15 μm, diameter = 2 μm) on ITO-glass substrate. (b) Schematic of the dip-in liquid lithography printing mode of 2-photon polymerization. (c) A schematic of the cell and nematic director around a microrod. (d) Polarized optical microscopic image of a microrod (length = 5 μm, diameter = 2 μm) under red-plate. Scale bar: 5 μm.

LC cell was observed under an upright polarizing microscope (Nikon Eclipse E600 POL). Red plate imaging was performed by inserting a full-wave retarder between crossed polarizers, as described elsewhere.[30] Videos and images were captured with Panasonic Lumix DC-G9, FLIR BFS-U3-80S5C-C and FLIR BFS-U3-16S2C-CS cameras. The FLIR cameras were typically synchronized at the rising edge of the AC voltage. Particle tracking in 2D images was performed using Fiji's (ImageJ) trackmate[44,45] and MATLAB was used for data analysis.

The effective viscosity η of MLC-6608 as a function of the shear rate $\dot{\gamma}$ in the range of $0.1\ s^{-1} \leq \dot{\gamma} \leq 100\ s^{-1}$ is measured at two temperatures, T = 21 °C and 25 °C, using an Anton Paar Rheometer MCR-302 with cone-plate geometry. The plate diameter is 60 mm and the cone angle is 1°. Each measurement is performed in the steady-state regime after the shear is applied for at least 10 s, assuring that the variation of the measured viscosity with time is less than 3%. Each η data point represents an average of six measurements.

The fluorescent confocal imaging was performed using a CrestOptics X-LIGHT V2 Confocal Imager, using a LED light source of 518 nm wavelength to excite the fluorescence of the sample with a 100× objective (Plan Apo λ 100× Oil NA = 1.45). The unit is attached to the side port of the Nikon Eclipse microscope. The tracking measurements to obtain 3D trajectories of the microrods were performed using image stacks of 2D plane projections of the *xy*, *yz*, and *xz* planes. The maximum image dimension is about 139 μm × 139 μm with a resolution of 2048 × 2048 pixels. We used a cropped image stack for our experiments typically in the range of 100 μm. The neighboring images in the *z*-stack are separated by 500 nm. For a cell of 10 μm thickness, a *z*-stack of about 14 μm is measured which is separated by 500 nm, allowing a good spatial resolution of 260 nm in the *xy* plane and 490 nm in the *z*-direction. The imaging volume is 100 μm × 40 μm × 15 μm, and each 3D fluorescent image of the whole imaging volume was taken in 1 second. The illumination time of individual 2D images of the *z*-stack was 10 ms.

3 Results and discussion

3.1 Brownian motion of rods with different aspect ratios

We first study how the aspect ratio of the microrods, which are aligned along the nematic director, affects their Brownian motion. For each aspect ratio, we captured videos with 25 000 frames at 10 fps of a stationary, but not immobilized, microrod in a planar cell with director $\hat{n}_0$ (1, 0, 0). The total time duration of video capturing is 2500 seconds or 41 minutes and 40 seconds, which requires very stable laboratory conditions in terms of temperature, air-flow and acoustic noise. After tracking the particle's position, we calculate the particle's displacement values for each frame and plot histograms showing the distribution of displacement along and perpendicular to the director for different time differences. We noticed that the width of the histograms, which is proportional to the diffusion coefficient, depends on the time difference chosen. This means that the diffusion coefficient depends on the time difference and indicates anomalous diffusion, which was first observed in liquid crystals by Turiv *et al.*[47] The diffusion coefficients are highest for the shortest time difference of 100 ms, and decrease to practically constant values in the time interval 1–3 s, which indicates the super-diffusion regime at short times.[47] The difference in diffusion coefficients at short and long time differences increases with the aspect ratio of the microrods. In what follows, we consider the values of the diffusion and frictional coefficients in the time interval of τ = 1–3 s.

Histogram distribution of displacement values along the rubbing direction ($n_{\parallel}$) and perpendicular ($n_{\perp}$) to the rubbing direction are plotted with the time difference of 2 s (τ = 2 s). This means that from 25 000 frames we chose frames that separated in time for 2 s, which at the frame rate of 10 fps means that we chose every 20th frame. This leaves us with 1250 frames, which are each separated by a time difference of 2 s. The displacement distribution plots are given in Fig. 2(d)–(f) for different aspect ratios of the microrods. Table 2 represents the measured values of diffusion constant parallel ($D_{\parallel}$) and perpendicular ($D_{\perp}$) to the rubbing direction. They are calculated from $\rho(x,\tau) = \frac{N}{\sqrt{4\pi D\tau}} e^{\frac{-x^2}{4D\tau}}$, where we get the diffusion values from the width of the Gaussian distribution for particular τ. These values were then averaged over the time interval of τ from 1 to 3 s and the error was calculated as well. The frictional coefficients $\gamma_{||}$ and $\gamma_{\perp}$ are calculated from the Stokes–Einstein relationship: $\gamma_{\parallel/\perp} = \frac{k_B T}{6\pi D_{\parallel/\perp}}$[30,46] where the temperature is T = 22 °C and k_B is the Boltzmann constant. Table 2 clearly shows the diffusion constant $D_{||}$ is higher along the director than $D_{\perp}$ perpendicular to it for all aspect ratios of the rods, and the frictional coefficients are significantly higher in the perpendicular direction $\gamma_{\perp}$ compared to along the director $\gamma_{||}$ for all aspect ratios. The diffusion constant, both parallel and perpendicular to the director, decreases with increasing aspect ratio of the microrod while the frictional coefficients increase for the higher aspect ratio of the microrod. We conjecture this is because longer rods have a higher surface area for contact with the fluid which increases the resistance of motion due to drag. The nematic director may be an additional factor, which allows the microrod to diffuse along the rubbing direction relatively more easily than perpendicular to it due to the anisotropy in the viscosity of the LC.[30,46]

3.2 Brownian motion of microrods under an applied DC electric field

It is well known that a DC electric field, applied to a spherical dipolar colloidal particle in a NLC exerts an electric force due to the charge of the particle.[18,48,49] If the electric field is perpendicular to the confining surface, the particle will be pushed by the electric force towards the surface, until the separation to the surface is stabilized by the repulsive surface force due to elastic director distortion. We tested whether the application of a DC electric field, which pushes the dipolar particle towards the surfaces, has any effect on the Brownian motion of the particle close to the interface. This may be of importance for our experiments with electric field propulsion, described further on.

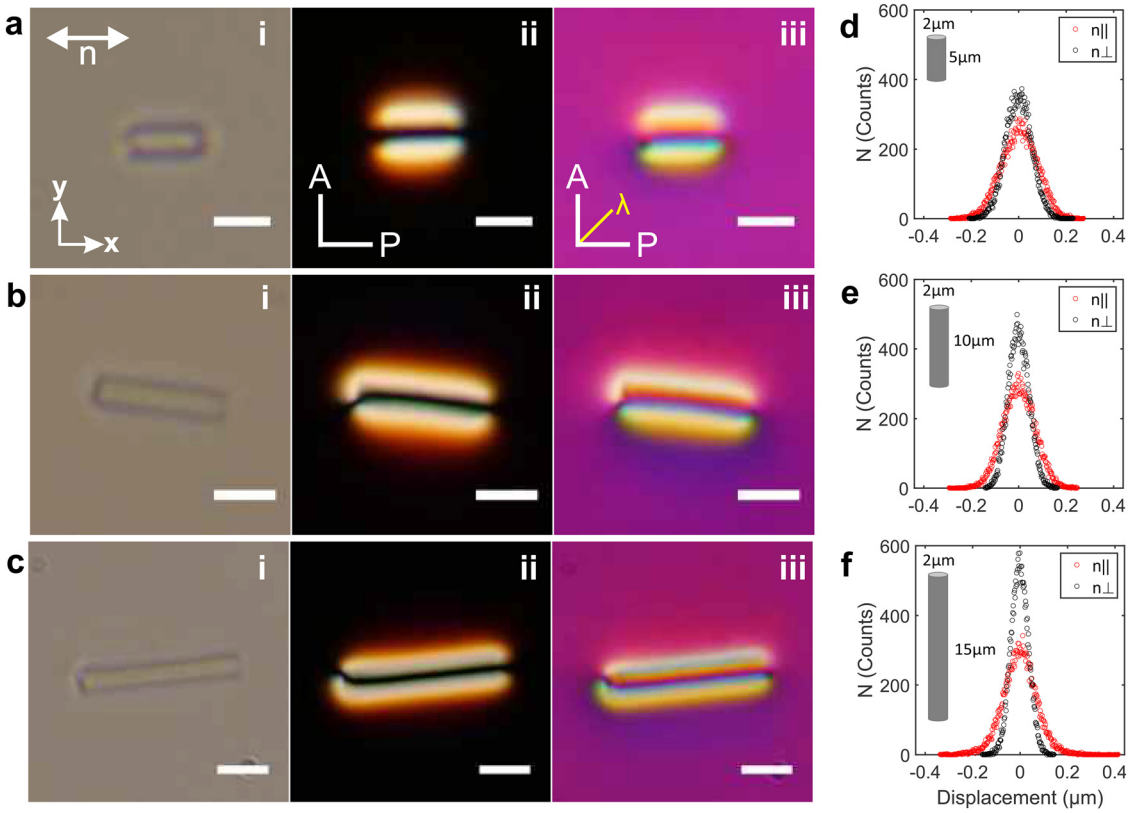

Fig. 2 POM images of the microrods with homeotropic surface anchoring under (i) polarized light, (ii) crossed polarizers, and (iii) red-plate for the (a) 2.5 aspect ratio microrod, (b) 5 aspect ratio microrod, and (c) 7.5 aspect ratio microrod in a planar cell. Scale bars: 5 μm. (d)–(f) Histogram representation of the distribution of displacement along the rubbing direction $n_{\parallel}$ and perpendicular to it $n_{\perp}$ for the microrod with aspect ratios of (d) 2.5, (e) 5, and (f) 7.5, all calculated for τ = 2 s.

Table 2 Aspect ratios of microrods and their respective diffusion constants, frictional coefficients measured along both parallel and perpendicular to the rubbing direction for time difference τ = 1–3 s. The diameter of the microrod is 2 μm for all aspect ratios and the cell thickness is 10 μm

Aspect ratio	$D_{\parallel}$ (m^2 s^{-1})	$\gamma_{\parallel}$ (kg s^{-1})	$D_{\perp}$ (m^2 s^{-1})	$\gamma_{\perp}$ (kg s^{-1})
5 : 2	$(1.32 \pm 0.02) \times 10^{-15}$	$(1.64 \pm 0.02) \times 10^{-7}$	$(6.8 \pm 0.1) \times 10^{-16}$	$(3.1 \pm 0.1) \times 10^{-7}$
10 : 2	$(1.1 \pm 0.1) \times 10^{-15}$	$(1.9 \pm 0.1) \times 10^{-7}$	$(4.5 \pm 0.2) \times 10^{-16}$	$(4.8 \pm 0.1) \times 10^{-7}$
15 : 2	$(1.0 \pm 0.1) \times 10^{-15}$	$(2.1 \pm 0.2) \times 10^{-7}$	$(3.2 \pm 0.1) \times 10^{-16}$	$(6.7 \pm 0.1) \times 10^{-7}$

We measured the diffusion constant of the microrod under an applied DC electric field (0, 0, E_z) normal to the cell and therefore perpendicular to the rubbing direction. A microrod of aspect ratio 5 with 10 μm length and 2 μm diameter in a planar cell with thickness 10.4 μm was studied. A video of 11 000 frames was recorded at 10 fps and the microrod's x and y positions were tracked which is used to measure its displacement values. We used the same method as previously described in Section 3.1 to calculate the diffusion constant and frictional coefficient from Brownian motion under an electric field, which are now shown in Table 3.

One can clearly see from Table 3 a significant decrease in the diffusion measured with and without a DC electric field. In all cases, both diffusion constants decrease when the electric field is applied. In other words, when the dipolar particles are pushed towards the cell surfaces by the electric force, their Brownian motion is hindered by an apparently increased friction and the particles are practically arrested. This effect is reversible and when the electric field is decreased to zero, the particles resume their Brownian motion.

Interestingly, there is a difference in the dipole colours in images taken with the red plate for each state shown in Table 3. Here, the top part of the cell is connected to the signal output while the bottom part is connected to the ground. In the case of a positive electric field 0.08 V μm^{-1}, the top part of the dipole is greenish-blue, while for a negative electric field −0.08 V μm^{-1}, the top part is orangish-yellow in the far field. It is also important to remember that when such a DC electric field is applied, the microrod moves along the direction of the electric field in the z-plane and is pushed towards the surface of the cell. The dipole colours therefore appear to be completely opposite to each other, which means that a red-plate image of a dipolar particle at the top interface is quite different from the red-plate image of the same particle at the bottom interface.

Table 3 Diffusion and frictional coefficients of microrods with the 10 : 2 aspect ratio measured under different DC electric fields applied perpendicular to the director calculated for τ = 1–3 s. The cell thickness of the planar cell is 10.4 μm. The polarized optical microscopic images were taken under a red-plate. Scale bar: 5 μm

E_{DC}	$D_{\parallel}$ ($m^2\ s^{-1}$)	$\gamma_{\parallel}$ ($kg\ s^{-1}$)	$D_{\perp}$ ($m^2\ s^{-1}$)	$\gamma_{\perp}$ ($kg\ s^{-1}$)	POM image
Off state	$(1.5 \pm 0.03) \times 10^{-15}$	$(1.44 \pm 0.03) \times 10^{-7}$	$(6.6 \pm 0.1) \times 10^{-16}$	$(3.3 \pm 0.1) \times 10^{-7}$	
0.08 V μm^{-1}	$(6 \pm 3) \times 10^{-17}$	$(4 \pm 1) \times 10^{-6}$	$(3 \pm 1) \times 10^{-17}$	$(8 \pm 3) \times 10^{-6}$	
0 V μm^{-1}	$(1.5 \pm 0.1) \times 10^{-15}$	$(1.5 \pm 0.1) \times 10^{-7}$	$(6.9 \pm 0.2) \times 10^{-16}$	$(3.2 \pm 0.1) \times 10^{-7}$	
−0.08 V μm^{-1}	$(4 \pm 2) \times 10^{-17}$	$(7 \pm 2) \times 10^{-6}$	$(2 \pm 1) \times 10^{-17}$	$(1.1 \pm 0.4) \times 10^{-5}$	
0 V μm^{-1}	$(1.4 \pm 0.1) \times 10^{-15}$	$(1.6 \pm 0.1) \times 10^{-7}$	$(4.1 \pm 0.2) \times 10^{-16}$	$(5.4 \pm 0.1) \times 10^{-7}$	

The *z*-position of the rod could also be observed under a polarizing optical microscope since the microrod moved out of focus, *i.e.* out of the *xy* plane. This displacement of particles along the electric field clearly indicates that the particles are spontaneously charged in the LCs. Similar sensitivity of the dipolar colours to the particle's height has also been observed by Y. Nishioka *et al.*[50] in the experiments using microspheres with homeotropic surface anchoring, forming topological dipoles in planar nematic cells.

3.3 Electric field propulsion of rods at low frequency (6 Hz and 11 Hz)

To propel the microrods in planar cells filled with MLC-6608 nematic LCs, an alternating electric field (0, 0, E_z) is applied to the planar cell perpendicular to the rubbing direction $\hat{n}_0$ (1, 0, 0) as presented in Fig. 1(c). The microrod typically moves with a velocity v_x, perpendicular to the direction of the applied AC electric field and along the nematic director, as shown in Videos S1 and S3. A similar propulsion of microrods was observed by Rasi *et al.*,[31] however those experiments were performed primarily at a higher field frequency of 50 Hz. In contrast, we investigate the microrod's propulsion at much lower frequencies, specifically 6 Hz, 11 Hz, and 90 mHz along with various aspect ratios of the microrods as an additional parameter. Here we present the complex behaviour of the microrods propulsion in detail.

Fig. 3 shows a time-series sequence of red-plate-polarizing optical micrographs of a typical microrod with an aspect ratio of 7.5, swimming with a frequency of (a) 6 Hz, and (b) 11 Hz at 0.66 V μm^{-1} electric field for approximately a single time period. The function generator triggers the camera such that image acquisition starts at the rising edge of the first waveform. One can immediately notice periodic changes in the colour pattern around the microrod, see also the detailed view in Video S2 in the SI. For example, panel 1 in Fig. 3(a) that was taken immediately after the rising edge of the waveform shows a typical ''quadrupolar'' colour pattern (blue-orange) that reverses colours in panel 5 taken immediately after the falling edge of the voltage waveform. In between (*i.e.* panels 4 and 7), the colour pattern is ''dipolar''-like. This alternating behaviour of quadrupolar colours is reminiscent of a similar colour pattern observed in electric field propulsion of solitary waves in NLCs, named ''directrons''.[41,42,51] The bright quadrupolar colours appear close to the rising and falling edge and transitions to a dipolar state eventually. Although these colour patterns suggest quadrupolar-like director distortions around the microrods, it is important to note that these colour patterns are not due to the quadrupolar distortion of the director field around the microrod, as will be shown and discussed further on. For simplicity, we define this period of quadrupolar-like distortions as the ''quadrupolar-like regime''. They typically start to appear above the threshold electric field, which is the electric field at which the microrod starts to move at a significant velocity. From the image sequence, it can also be observed that the microrod goes in and out of focus within a single time-period, which means that the microrod moves in the *z*-plane, *i.e.* along the applied electric field.

We have already mentioned that whenever the field direction reverses, the quadrupolar colour pattern reverses and then gradually transforms into a dipolar-like colour pattern. In addition, it can be clearly seen that the dipolar colour pattern reverses, when the polarity of the electric field reverses. For example, in Fig. 3(a) we can see at 71 ms the blue colour is at the top of the dipole and the orange color is below the colloid. Looking at the same colloid at 143 ms, the orange color is now at the top of the colloid and the blue color is under the colloid: the colors of the dipolar colloid have interchanged. This is similar to the case of 11 Hz shown in Fig. 3(b), where the blue-orange at the top of the dipole at 41 ms is reversed at 92 ms, where it is orange-blue.

Fig. 3(c) and (d) show the time dependence of the *x* and *y* positions of the microrod, respectively. Both positions are clearly

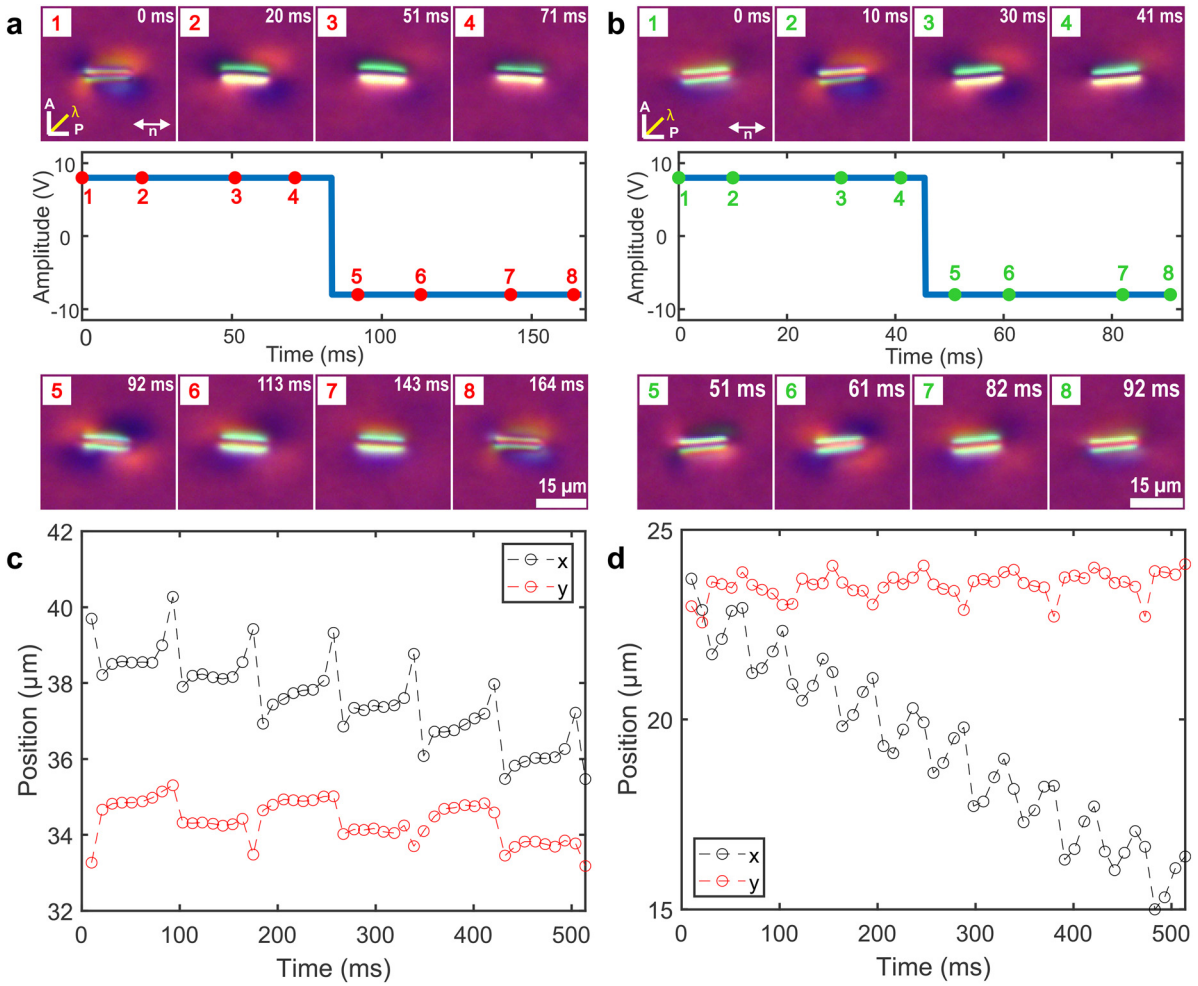

Fig. 3 Image sequence of the microrod with aspect ratio 7.5 swimming at (a) 6 Hz, and (b) 11 Hz and 0.66 V µm^{-1} for a single period, with the first image synchronized at the rising edge of the waveform. The images are taken under a red-plate and were captured at 97 fps. Representation of the microrod's x and y positions over time at (c) 6 Hz and (d) 11 Hz. The x-position is indicated by black circles, and the y-position is indicated by red circles. No electrohydrodynamic convection (EHC) patterns were observed up to 4 V µm^{-1}, indicating that the EHC threshold lies above this field strength.

time-periodic and show abrupt changes whenever the electric field changes the sign. A similar periodicity in position was also reported by Senyuk *et al.*[28] In addition, the x-position of the microrod clearly shows a constant drift of the microrod along the director and therefore along the direction of the microrod, which reflects swimming of the microrod due to the action of the electric field. The swimming velocity is clearly higher at the higher frequency of 11 Hz.

To further study the electric-field dependence of the velocities of the microrods, we measured the absolute velocities of microrods for both cases 6 Hz and 11 Hz, as a function of the electric field strength. Fig. 4 shows the absolute velocity *vs.* electric field plots in double logarithmic scale, where the velocities are an average velocity over 4–5 consecutive measurements. There are three different aspect ratios of microrods, *i.e.* 2.5, 5, and 7.5 represented in Fig. 4(a)–(c), respectively. We observed that the threshold for swimming was around ~0.1 V µm^{-1}. We can see from Fig. 4(a)–(c) that the absolute velocity shows third to fifth order power-law dependencies on the electric field. A typical LCEEP exhibits quadratic dependence of velocity V_x on electric field E_z,[16] which is not the case here. Recently, Rajabi *et al.*[22] showed a higher order of four and six dependencies of the velocities on the electric field, the reasoning behind which was the shear-thinning effect of liquid crystal.

To check if the contributing factor is the shear-thinning effect of the liquid crystal, we measured the viscosity dependence on the shear rate of MLC-6608 liquid crystal at 21 °C and 25 °C, as shown in Fig. 4(d). One can see a strong shear-thinning behavior of the viscosity of MLC-6608 for shear rates in the range of 0.1 s^{-1} < $\dot{\gamma}$ < 1 s^{-1} and a moderate shear-thinning in the intermediate range 1 s^{-1} < $\dot{\gamma}$ < 10 s^{-1}; the response becomes practically Newtonian at higher shear rates $\dot{\gamma}$ > 10 s^{-1}. The viscosity change with shear rate is well fitted by a universal function $\eta = a\dot{\gamma}^{\beta} + b$, where a = 0.6 mPa s$^{0.14}$, β = −0.86, b = 27.8 mPa s at 21 °C and a = 1.3 mPa s$^{0.2}$, β = −0.80, and b = 22.2 mPa s at 25 °C. The reason for shear thinning here is the flow-aligning character. Although this higher order dependence phenomena cannot be completely explained by shear-thinning alone, but it can be said that it does have a contribution based on the previous results by Rajabi *et al.*[22]

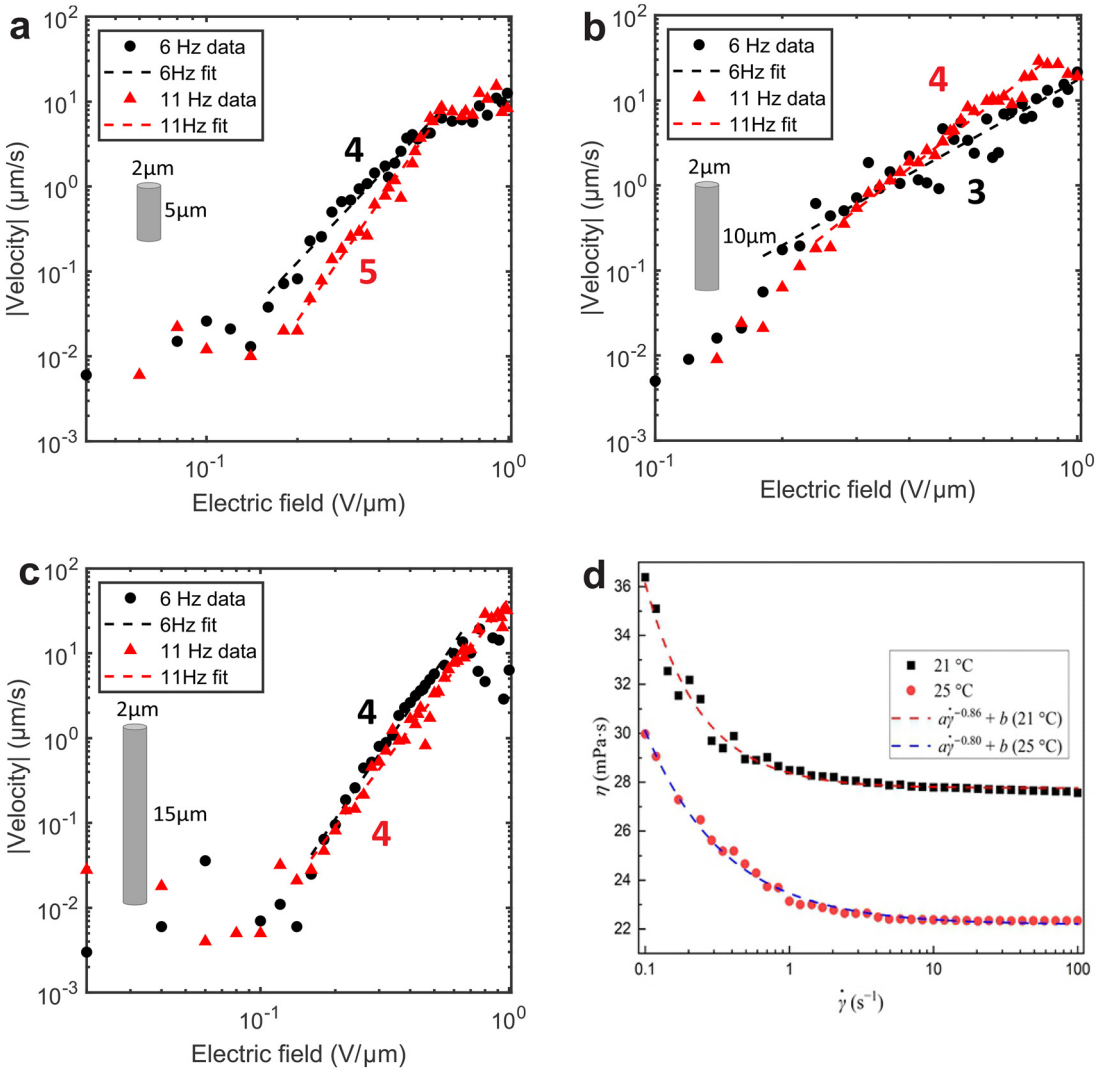

Fig. 4 Log–log plots of absolute velocity as a function of electric field of microrods along the x-direction for the (a) 2.5 aspect ratio, (b) 5 aspect ratio, and (c) 7.5 aspect ratio with 10 μm cell thickness, with the dashed lines representing a linear fit. All the microrods were printed with IP-Dip polymer. The numbers 3, 4, and 5 in the individual plots indicate the values of the power law exponent α, where $v_x \sim E_z^{\alpha}$. AC voltages of the square waveform were applied perpendicular to the planar cell. The velocities are measured as an average over 4 particle velocities for 6 Hz and over 5 particle velocities for 11 Hz. (d) Measured viscosity η of MLC-6608 as a function of shear rate $\dot{\gamma}$ at 21 °C and 25 °C.

3.4 Electric field propulsion of rods at ultra-low frequency: polarized and fluorescence confocal imaging in 3D

It is very clear from the microscope observations of the microrods' swimming that the motion of microrods is more complex than simple translation of the center of mass of the microrod along the director. There is clear evidence of sideways motion at the moment when the electric field changes sign, and clear evidence of microrods tilting and moving out of focus during the steady field. To investigate further this rather complicated movement and to clarify what actually happens in the so-called 'quadrupolar regime swimming', we reduced the frequency of the electric field even lower to 90 mHz. This increases the time period of observation of the changes that occur in the system and makes it possible not only to follow more accurately the particle motion in 2D images, but also to perform 3D confocal images and measure the full 3D trajectory of the microrod. The first image of the image sequence was synchronized to the rising edge of the applied electric field, such that the amplitude of the electric field values can be correlated to the changes of the director distortions.

Fig. 5(a) shows the POM image sequence of a 5 aspect ratio microrod, swimming with an applied electric field of 0.1 V μm^{-1} and a frequency of 90 mHz. One can clearly see that the first quadrupolar-like state can be observed within ~18% of the positive half-cycle (*i.e.* at ~1 s) and within the first ~13% of the time of the negative half-cycle for a square waveform. The dipole colours appear to flip back and forth for every half-cycle. The top bluish-green colour of the dipole changes to yellowish-orange, and similarly, the bottom orangish-yellow colour changes to blue colour in the far field within half a cycle. The dipole colours return back to its initial state towards the negative half cycle. It can also be clearly noted

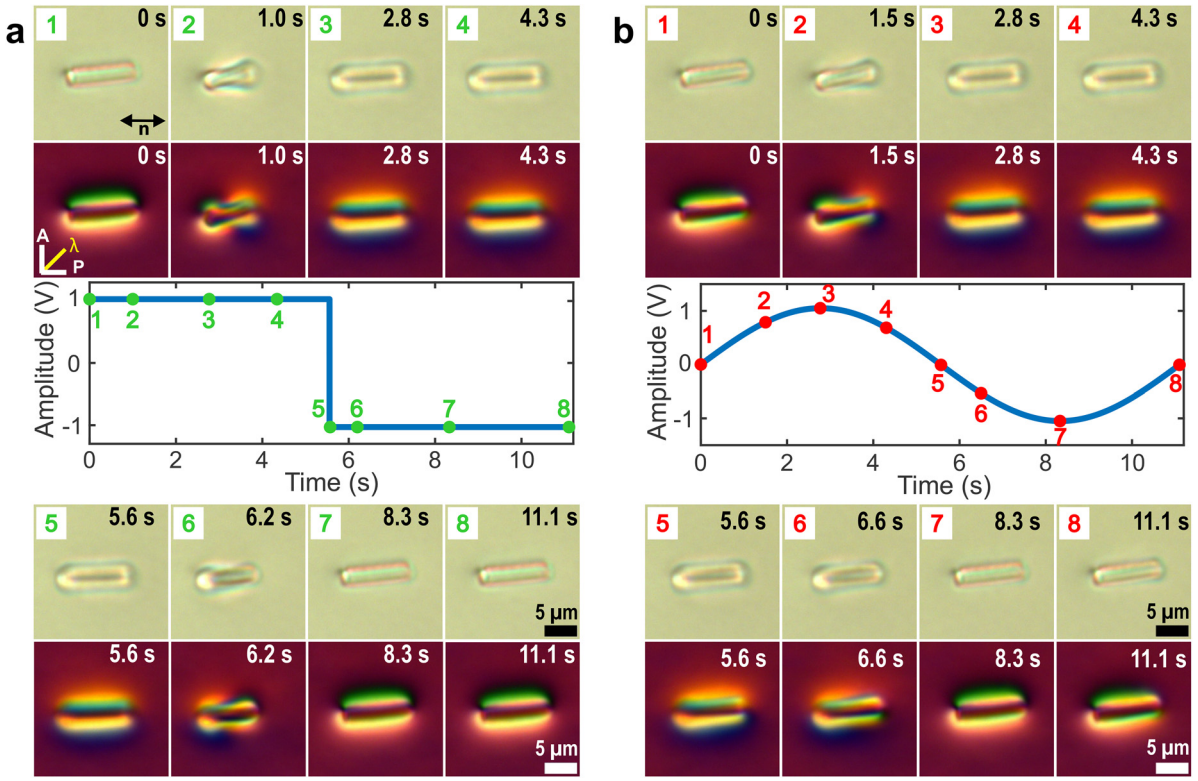

Fig. 5 Synchronized POM image sequences of a 5 aspect ratio microrod swimming at an electric field of 0.1 V µm^{-1} and frequency of 90 mHz. The images were taken under polarized light and red-plate for (a) square waveform and (b) sinusoidal waveform. The cell thickness here is 10 µm and the frame rate is 30 fps. No electrohydrodynamic convection (EHC) patterns were observed up to 4 V µm^{-1}, indicating that the EHC threshold lies above this field strength.

here that the two "states" of dipole appear to be of different focal plane, similar to what we observed in Fig. 3. This suggests the motion of the microrod in the *z*-plane, *i.e.*, from one LC–glass interface to another, accompanied by the tilting of the microrod, also clearly seen in panels 2 and 6 of Fig. 5(a).

To study the quadrupolar-like distortions around the microrod for electric fields at low frequency, such as 90 mHz with square waveform, is challenging since the microrods would often get stuck at the walls. For this reason, we switched to a sinusoidal waveform since the amplitude change is gradual and the probability of sticking to the surface is reduced. Fig. 5(b) shows the quadrupolar behaviour for sinusoidal waveform at 90 mHz and 0.1 V µm^{-1}. We observe similar dipolar to quadrupolar transitions with a sinusoidal waveform. Here, for the first transition between the two dipole states, it takes about 34% of the time of the first positive half cycle while simultaneously undergoing slow changes to the quadrupolar distortion colours. In the case of the negative half cycle, the dipole to dipole transition takes 28% of the half cycle time. The images under the red-plate can be compared to the images under the polarized light. The images under the polarized light clearly show tilt at 1 s for Fig. 5(a) and 1.5 s for Fig. 5(b), which could be observed from the obvious change in the length of the microrod.

We conclude from red-plate images in Fig. 3 and 5 that the quadrupolar colour pattern around the microrod appears immediately after the switching of the sign of the electric field. It seems to be a transient phenomenon most likely related to the transient ionic flow, which induces transient tilting of the microrod. On the other hand, this transient tilting is followed by the up or down movement of the particle, which is responsible for alternating of the yellow/blue coloured images after the particle's height is stabilized and the particle adopts the colour pattern of a dipolar director structure.

To investigate the tilting motion of the microrod in detail, we recorded its motion in 3D over time using confocal microscopy. Here the experiments were performed with 5 aspect ratio microrods at 90 mHz with sinusoidal waveform in a 10 µm planar cell. After performing several experiments on the same sample and imaging the swimming of different microrods we concluded that there are two classes of microrod swimmers: a fast one and a slow one, as explained in what follows. Fig. 6 shows the confocal data of a "slow" microrod with 5 aspect ratio swimming at an average velocity of −0.08 µm s^{-1} along the *x*-direction, at a driving field of 0.56 V µm^{-1}, see also Video S4. Fig. 6(a) shows the image sequence of the microrod motion in the *xz* cross-section of the sample for a single period of the electric field, where the coloured circles represent the tracking points from the center of mass of the microrod over time. The images clearly reveal the tilting of the microrod, confirming the behaviour observed for a different case in the polarized optical images presented in Fig. 5. The time-dependence of the tilt angle $\varphi(t)$

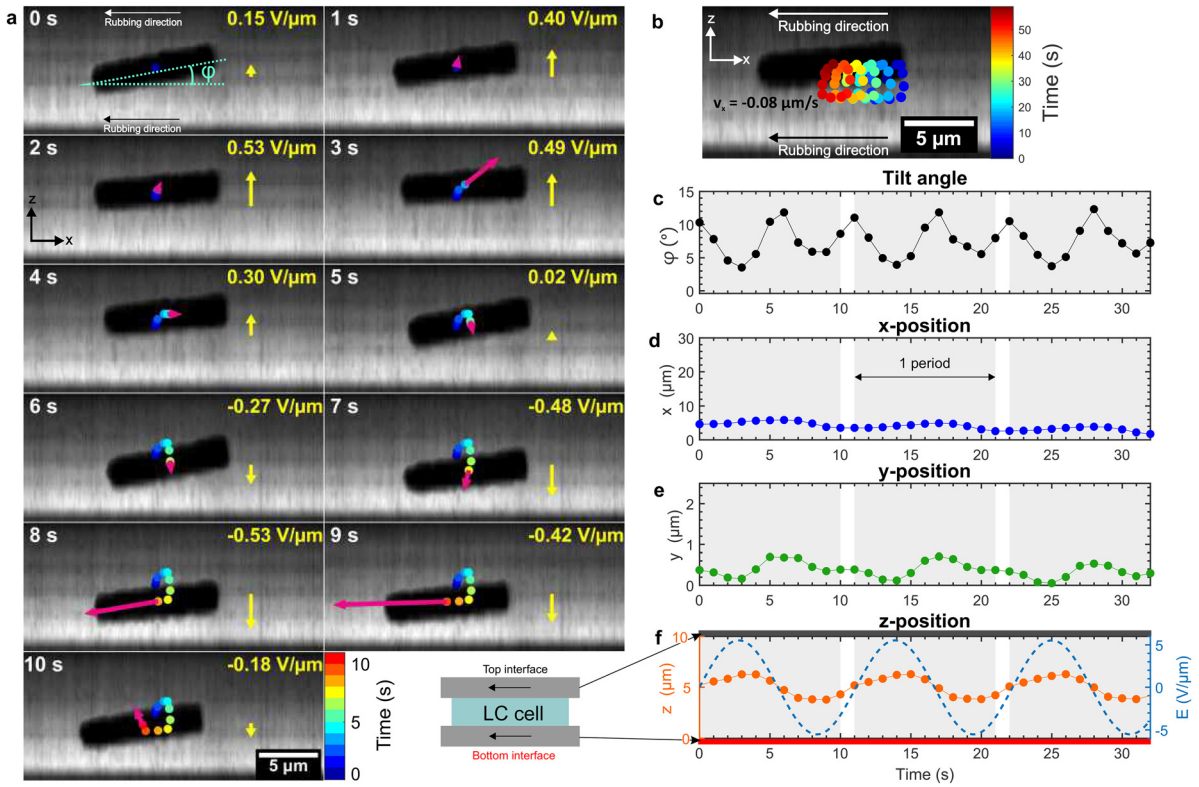

Fig. 6 Confocal imaging data of a 5 aspect ratio microrod swimming at 0.56 V μm^{-1} with 90 mHz frequency, sinusoidal waveform in a 10 μm thick planar cell. The swimming velocity is very low, $v_x = -0.08$ μm s^{-1}. (a) Image sequence of the projection of a microrod swimming for a single period of frequency in the *xz* plane. The pink arrows on the images represent instantaneous velocity of the center of mass. (b) Trajectory of the microrod in the *xz* plane, colour coded over time. (c) Tilt angle of the microrod as a function of time. (d) *x*-Position as a function of time. (e) *y*-Position as a function of time. (f) Time dependence of the electric field and the *z*-position of the microrod.

shown in Fig. 6(c) demonstrates that the tilt angle is always positive with rather strong variation in time. The periodicity of the tilt is doubled compared to the period of driving electric field, which indicates quadratic (*i.e.* dielectric) coupling between the tilt and the field. On the other hand, there is clearly a linear relationship between the motion of the microrod and the applied electric field (refer to Fig. 6(d)–(f)). This is more pronounced in the case of *x*-position (*i.e.* along the director) in Fig. 6(d) and *z*-position in Fig. 6(f). The microrod moves back and forth along the *x*-axis, while slowly drifting along the *x* direction (refer to Fig. 6(d)) with a net velocity of −0.08 μm s^{-1}. The microrod moves about 2.4 μm up and down in the *z*-plane in a periodic oscillatory motion with time. For the *y*-position, the difference between the back and forth motion appears to be an order of magnitude smaller than compared to that of the ones in *x* or *z* positions. Fig. 6(b) represents a *xz* projection of the microrod's motion for longer time period of about 60 seconds. The trajectory of the microrod reveals a helical-like motion which is later confirmed by the 3D trajectory in Fig. 7.

In the second case, shown in Fig. 8, we observed a "fast" swimming microrod with a different trajectory pattern for the same value of applied electric field. Here, the microrod propels at −0.5 μm s^{-1} in the *x*-direction, see also Video S5. The image sequences of the microrod in the *xz* plane in Fig. 8(a) reveals a swinging-like motion with the bright pink coloured arrows pointing out the direction of the propulsion. The microrod clearly displays a tilting motion at a doubled frequency, as shown in Fig. 8(c). The positions along the *x*, *y*, and *z* coordinates in Fig. 8(d)–(f) share a similar linear relationship to the frequency of the electric field applied. Fig. 8(b) reveals a swinging-like trajectory in the *xz*-plane over a longer period of time of one minute and also is observed in 3D trajectory represented in Fig. 9. Fig. 8(b) illustrates how the microrod only slightly moves backward before propelling forward, without completing a full circular motion. In both the examples in Fig. 6(f) and 8(f), the *z*-position over time is sinusoidal.

4 Discussion

Most of the studies of colloidal swimming in nematic LCs were focused on the relationship between the swimming velocity and the magnitude of the electric field, whereas less attention has been paid to the temporal analysis of the trajectories of the propelled particles. This is because full 3D tracking of particles in LCs is only possible by using the fluorescent confocal microscopy that is capable of measuring all three coordinates of the particle. An exception is the work of Sasaki *et al.*,[52] who reconstructed the time dependence of the *z*-trajectory of microspheres, swimming in negative dielectric anisotropy LCs under

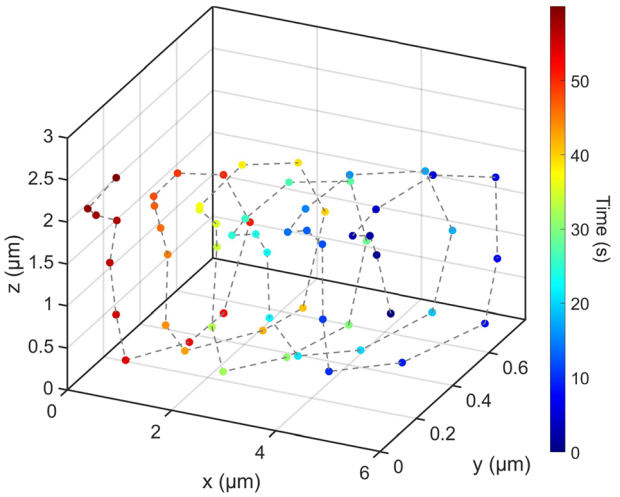

Fig. 7 Trajectory of the microrod swimming at 0.56 V μm^{-1} and 90 mHz, with positions colour-coded by time. This trajectory corresponds to Fig. 6, the swimming velocity is $v_x = -0.08$ μm s^{-1}.

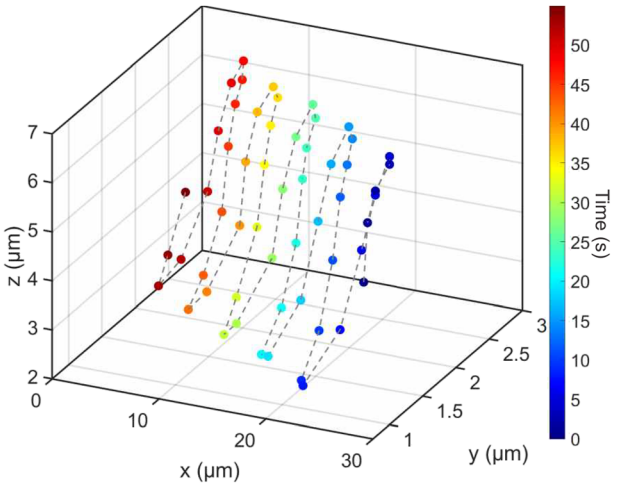

Fig. 9 3D trajectory of the microrod swimming at 0.56 V μm^{-1} and 90 mHz, with positions colour-coded by time. This trajectory corresponds to Fig. 8, the swimming velocity is $v_x = -0.5$ μm s^{-1}.

the influence of the electric field. They observed similar up and down movement (*i.e.* along the *z*-axis, which is similar to our coordinate system setting), in combination with steady swimming along the nematic director.

Our confocal images of the microrod's swimming at very low frequency of the applied electric field reveal interesting details about colloidal propulsion of microrods, as shown in Fig. 6 and 8. In both cases, the center of mass of the microrod experiences an up and down movement (*i.e.* along the electric field direction) with a time period that is exactly equal to the period of the electric field, see Fig. 6(f) and 8(f). This clearly indicates a linear coupling of the *z*-position of the microrod's center of mass to the applied electric field, clearly indicating that the microrod in the LC is electrically charged.

The up and down movement of the center of mass of the microrod is accompanied by the synchronized tilting of the

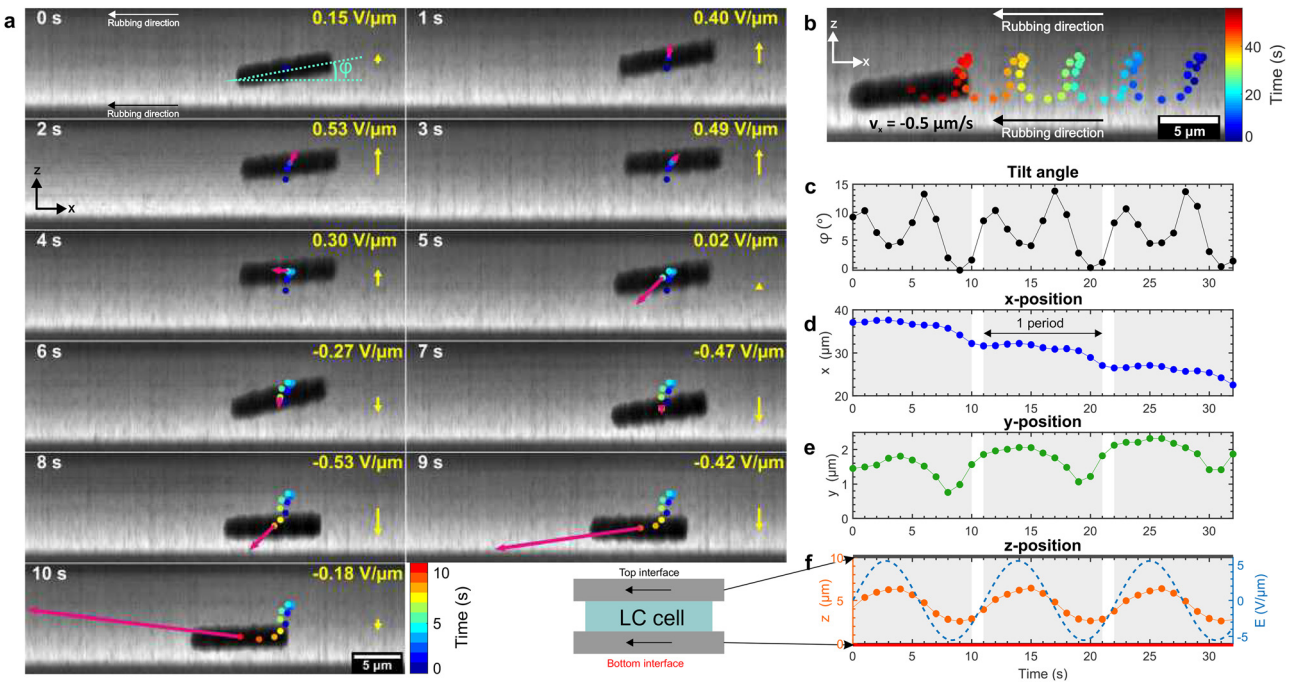

Fig. 8 Confocal data of a 5 aspect ratio microrod swimming at 0.56 V μm^{-1} with 90 mHz frequency, sinusoidal waveform in a 10 μm thick planar cell. The swimming velocity is very high $v_x = -0.5$ μm s^{-1}. (a) Image sequence of the projection of a microrod swimming for a single period of frequency in the *xz* plane. The pink arrows on the images represent instantaneous velocity of the center of mass. (b) Trajectory of the microrod in the *xz* plane colour coded over time. (c) Tilt angle of the microrod as a function of time. (d) *x*-Position as a function of time. (e) *y*-Position as a function of time. (f) Time dependence of the electric field and the *z*-position of the microrod.

microrod in the applied electric field, which is shown in better detail in Fig. 6(c) and 8(c). In both cases, the tilt angle of the microrod is always positive and it oscillates with a frequency that is doubled compared to the frequency of the applied electric field. This is a clear indication of the dielectric coupling of a polarizable microrod in an external field, which was discussed in several works.[31] Briefly, an extended 1D object such as a microrod shows larger electric polarizability when the electric field is applied along the rod, compared to the transverse direction. This shape anisotropy is therefore translated into dielectric anisotropy of the microrod, which tends to align along the electric field direction. Because of the polarizability and dielectric–quadratic coupling between the rod's direction and the electric field, the rod does not reorient when the direction of the electric field is reversed. Next, we note from Fig. 6(d), (e) and 8(d), (e) that microrods experience propulsion in the x-direction (along the far field direction) and the y-direction (perpendicular to the far field direction). These trajectories show acceleration in both x and y directions, indicating forces that are linear in the applied field. However, the movement and acceleration in the lateral, y-direction, are at least one order of magnitude smaller compared to those in the x-direction. It is clear from the analysis of temporal behaviour of the $x(t)$, $y(t)$ and $z(t)$ coordinates that the swimming of microrods under an external electric field is dictated by the combination of a linear and quadratic coupling of the electric field with the charged microrod and the director field around the microrod. Here the linear coupling is due to the electric charge of the particle and flexoelectric polarization of the distorted director field around the particle. At low frequency, the microrod would have enough time to move along the z-coordinate and at higher frequencies this motion would decrease since there would be less time for the microrod to respond.

The sinusoidal up and down motion of the microrod when exposed to an AC electric field appears to be connected to the change of director colours around the microrod. Based on the experiments performed at 90 mHz, the director colours of the microrod appears to change between different dipole states of director colours with an intermediate 'quadrupolar-like' state, which corresponds to the tilt of the microrod.

The tilt angle measurements of the microrod in Fig. 6(c) and 8(c) show that within a single period, the tilt angle is the highest only once. This supports the reason why the quadrupolar colours of the microrod for positive and negative half-cycles need not be exactly mirror symmetric to each other (refer to Fig. 5). Since the waveform of the AC electric field is symmetric, this does not explain the asymmetry in tilt angle peak within a single period. The possible reasons could be due to sedimentation, colloid–wall interactions, geometry of the microrod, anisotropy in viscosity, elasticity, and the electro-hydrodynamics of the surrounding medium or a combination of these parameters. Rasi *et al.*[31] reported that in nematic LCs, the reason behind the tilt of the microrod under an AC electric field is the competing forces of elastic and induced electrostatic torque.[31]

The dipolar-like director structure with a hedgehog defect on one end should in principle act as a permanent electric dipole because of uneven distribution of ionic and flexoelectric charges. It is therefore expected that in an applied electric field, the microrod would tend to rotate into the direction of the field because of two mechanisms: (i) a linear coupling of the external electric field with a permanent electric dipole moment of the micro-rod, and (ii) dielectric–quadratic coupling of the field with induced charges. The confocal measurements of the microrod's tilt angle, presented in Fig. 6(c) and 8(c), clearly show that the electric field induced tilt is quadratic in the field. However, it is also clearly seen that during the second half period (when the electric field is negative), the maximum tilt angle is systematically different from the maximum tilt angle for the positive electric field. This asymmetry of tilt amplitudes within a single period of electric field oscillation could be an indication of the linear coupling of external electric field with the permanent electric dipole of the microrod.

Initially, the defect change from dipolar to quadrupolar and back and forth was thought to be the possible reason behind the director colour change but we found out that this wasn't the case. We did not observe any Saturn ring defect which are typically dark circles around the microrod during the transition of the director reorientation along the length of the microrod. Other systems where similar behaviours are found include the colour-changing behaviour of propelled quasi-particles, which is often observed in LC systems that exhibit directions (particle-like solitary waves),[40,41] dressed colloids, *i.e.* an oscillating director reorientation patterns around the colloid that are linear to the frequency of the electric field applied,[51] and have a threshold. The director deformation is typically smooth and extends over a couple of length scales of the diameter of the microrod which can also be seen in our system. Although such topologically protected solitons are typically observed in (−, −) nematic LCs,[40,41,51] there are also reports that show solitons are also observed in (−, +).[42] Although this does appear to be quite close to what we observe in our system, we are not convinced that solitons are observed in our experiments. Rather than solitons, up and down movement of propelled particles, accompanied with tilting in the applied electric field, is probably responsible for dynamic colour changes.

We wondered if electro-hydrodynamic convection or flexoelectric effect could be the possible reasoning behind such motion and the director reorientation occurring since the LC has negative dielectric anisotropy and positive conductivity anisotropy. Previous reports have stated that colloids can be transported *via* EHC rolls,[50,52–54] but this appears to be quite different from our case. We could observe such EHC roll patterns on the edges of the cell, but not in the region of observation. In this region far from the edges, where the measurements were performed, the EHC patterns were not observed up to 4 V μm^{-1} at 6 Hz and 11 Hz for 10 μm thick cells. This indicates that the threshold is much higher. These EHC threshold values appear to be much higher than the threshold for propulsion which is 0.1 V μm^{-1}. The other not so well understood observation includes the random change of direction of motion of microrods at higher electric field strengths, which also depends on the frequencies. The microrod typically slows down before it changes the direction of motion.

The non-linear relationship between the electric field and velocity (v_x) of higher order appears to be complex. We expected the velocity of the microrod to increase with the length[11,16,18,31,55,56] which is observed in the case of 11 Hz but surprisingly did not contribute to a significant difference in the case of 6 Hz (refer to Fig. S4 in the SI). The confocal studies reveal that one of the major contributions of velocity (v_x) is the tilting motion. A longer microrod of 15 μm length will have more constraint in terms of space for the tilting motion in *z*-coordinate compared to that of a 5 μm length microrod with a fixed cell thickness of 10 μm. This could possibly be the reason why there is not a huge difference in the velocity (v_x) along the *x*-coordinate for different lengths of microrods at 6 Hz. At 11 Hz, the tilting motion would be reduced compared to that of 6 Hz since the electric field time scale would be relatively lower, giving the microrod relatively less time to move along the *z*-coordinate with the oscillating electric field. This makes sense why the velocity increases slightly with the increase in the aspect ratio of the microrods at 11 Hz, since the confinement due to the cell thickness will have relatively less influence compared to the case of 6 Hz. We also observed that the combination of rubbing direction on the two surfaces of the cell has an influence on the power law exponents that describe the electric field dependence of propulsion velocities. In the case of antiparallel cells, and especially for short microrods, the power-law exponent was around 9–10 (see Fig. S5b), which is significantly larger than in the parallel case.

5 Conclusions

More generally, this work demonstrates the capabilities enabled by complex fluids for the electric propulsion of micro-particles. Specifically, we show that by designing the particle geometry and/or the complex fluid structure (such as length, aspect ratio) one can alter not only the three-dimensional trajectories of the motile particles, but also the actual coupling strength between the particle velocity and the electric field, *i.e.* the power-law of the coupling. Actually, we observe that the electric, dielectric and flexoelectric coupling in rod-like nematic colloids is responsible for complex trajectories of propelled particles, which includes 3D periodic motion of the center of mass of the particles, synchronized with dynamic tilting. This clearly indicates that the propulsion of rod-like colloids in nematic LCs is governed not only by electrophoretic forces, but also structural forces due to director time-dependent oscillations, which induce flow of the nematic liquid crystal. The nature of electric field propulsion of microrods in nematic LCs is therefore highly anisotropic because of highly anisotropic ion dynamics, hydrodynamics, flexoelectricity and nematic elasticity, which are coupled to each other. The typical nonlinear nature of complex fluids indicates highly likely complex collective dynamics of such propelled particles that could include different stable/unstable and bound/unbound dynamical particle states and trajectories. Furthermore, the developed experimental methodology based on 3D printing of colloidal particles, has the potential to unravel a myriad of colloidal particle systems with diverse shapes, topologies and geometries.

Author contributions

L. J. S. R. conducted all experiments on microrods, analyzed the data, and wrote the manuscript. I. M. conceived the idea, supervised the overall research and contributed to writing the manuscript. M. R. co-supervised the research, revised the manuscript and contributed to writing the manuscript. A. C. D. performed the viscosity measurements, analyzed the results, and contributed to writing that section. V. J. and V. B. contributed to the dielectric and conductivity measurements of the liquid crystal. O. D. L. reviewed and edited the manuscript.

Conflicts of interest

There are no conflicts to declare.

Data availability

The data supporting this article have been included as a part of supplementary information (SI) and the raw data are available *via* Zenodo https://doi.org/10.5281/zenodo.17514240. Supplementary information is available. See DOI: https://doi.org/10.1039/d5sm01104c.

Acknowledgements

The authors would like to thank Damjan Svetin, Nanocenter, for providing the SEM images. L. J. S. R. and I. M. acknowledge the support from Slovenian Research and Innovation Agency, grant PR-10670. O. D. L. acknowledges the support from the US National Science Foundation, grant DMR-2341830.

References

1 I. Buttinoni, G. Volpe, F. Kümmel, G. Volpe and C. Bechinger, *J. Phys.: Condens. Matter*, 2012, **24**, 284129.
2 S. R. McCandlish, A. Baskaran and M. F. Hagan, *Soft Matter*, 2012, **8**, 2527.
3 J. Bialké, T. Speck and H. Löwen, *Phys. Rev. Lett.*, 2012, **108**, 168301.
4 I. Buttinoni, J. Bialké, F. Kümmel, H. Löwen, C. Bechinger and T. Speck, *Phys. Rev. Lett.*, 2013, **110**, 238301.
5 S. J. Ebbens and J. R. Howse, *Soft Matter*, 2010, **6**, 726.
6 C. Bechinger, R. Di Leonardo, H. Löwen, C. Reichhardt, G. Volpe and G. Volpe, *Rev. Mod. Phys.*, 2016, **88**, 045006.
7 S. Ramaswamy, *Annu. Rev. Condens. Matter Phys.*, 2010, **1**, 323–345.
8 I. S. Aranson, *Phys.-Usp.*, 2013, **56**, 79–92.
9 T. M. Squires and M. Z. Bazant, *J. Fluid Mech.*, 2004, **509**, 217–252.
10 T. M. Squires and M. Z. Bazant, *J. Fluid Mech.*, 2006, **560**, 65–101.
11 O. D. Lavrentovich, *Curr. Opin. Colloid Interface Sci.*, 2016, **21**, 97–109.
12 I. Lazo, C. Peng, J. Xiang, S. V. Shiyanovskii and O. D. Lavrentovich, *Nat. Commun.*, 2014, **5**, 5033.

13 B. Senyuk, Q. Liu, S. He, R. D. Kamien, R. B. Kusner, T. C. Lubensky and I. I. Smalyukh, *Nature*, 2012, **493**, 200–205.
14 B. Jérôme, *Rep. Prog. Phys.*, 1991, **54**, 391–451.
15 H. Stark, *Phys. Rep.*, 2001, **351**, 387–474.
16 O. D. Lavrentovich, I. Lazo and O. P. Pishnyak, *Nature*, 2010, **467**, 947–950.
17 A. V. Ryzhkova, F. V. Podgornov and W. Haase, *Appl. Phys. Lett.*, 2010, **96**, 151901.
18 I. Lazo and O. D. Lavrentovich, *Philos. Trans. R. Soc., A*, 2013, **371**, 20120255.
19 S. Gangwal, O. J. Cayre, M. Z. Bazant and O. D. Velev, *Phys. Rev. Lett.*, 2008, **100**, 058302.
20 M. Z. Bazant and T. M. Squires, *Phys. Rev. Lett.*, 2004, **92**, 066101.
21 C. Peng, I. Lazo, S. V. Shiyanovskii and O. D. Lavrentovich, *Phys. Rev. E: Stat., Nonlinear, Soft Matter Phys.*, 2014, **90**, 051002.
22 M. Rajabi, T. Turiv, B.-X. Li, H. Baza, D. Golovaty and O. D. Lavrentovich, *Phys. Rev. Lett.*, 2024, **132**, 158102.
23 I. Dierking, G. Biddulph and K. Matthews, *Phys. Rev. E: Stat., Nonlinear, Soft Matter Phys.*, 2006, **73**, 011702.
24 D. K. Sahu, S. Kole, S. Ramaswamy and S. Dhara, *Phys. Rev. Res.*, 2020, **2**, 032009.
25 D. K. Sahu and S. Dhara, *Phys. Fluids*, 2021, **33**, 087106.
26 V. S. Devika, D. K. Sahu, R. K. Pujala and S. Dhara, *Phys. Rev. Appl.*, 2022, **18**, 014030.
27 B. Senyuk, R. E. Adufu and I. I. Smalyukh, *Langmuir*, 2022, **38**, 689–697.
28 B. Senyuk, J.-S. Wu and I. I. Smalyukh, *Proc. Natl. Acad. Sci. U. S. A.*, 2024, **121**, e2322710121.
29 I. Muševič, *Liquid Crystal Colloids*, Springer, 2017.
30 U. Tkalec, M. Škarabot and I. Muševič, *Soft Matter*, 2008, **4**, 2402–2409.
31 M. R. Muhammed, S. Archana, R. K. Pujala and S. Dhara, *Soft Matter*, 2022, **18**, 6043–6050.
32 T. Hueckel, G. M. Hocky and S. Sacanna, *Nat. Rev. Mater.*, 2021, **6**, 1053–1069.
33 T. Tigges and A. Walther, *Angew. Chem., Int. Ed.*, 2016, **55**, 11261–11265.
34 S. Riedel, L. A. Hoffmann, L. Giomi and D. J. Kraft, *Nat. Commun.*, 2024, **15**, 5692.
35 R. P. Doherty, T. Varkevisser, M. Teunisse, J. Hoecht, S. Ketzetzi, S. Ouhajji and D. J. Kraft, *Soft Matter*, 2020, **16**, 10463–10469.
36 A. Martinez, M. Ravnik, B. Lucero, R. Visvanathan, S. Žumer and I. I. Smalyukh, *Nat. Mater.*, 2014, **13**, 258–263.
37 S. M. Hashemi, U. Jagodič, M. R. Mozaffari, M. R. Ejtehadi, I. Muševič and M. Ravnik, *Nat. Commun.*, 2017, **8**, 14026.
38 Y. Yuan, A. Martinez, B. Senyuk, M. Tasinkevych and I. I. Smalyukh, *Nat. Mater.*, 2017, **17**, 71–79.
39 M. Nikkhou and I. Muševič, *Soft Matter*, 2018, **14**, 9819–9829.
40 B.-X. Li, V. Borshch, R.-L. Xiao, S. Paladugu, T. Turiv, S. V. Shiyanovskii and O. D. Lavrentovich, *Nat. Commun.*, 2018, **9**, 2912.
41 B.-X. Li, R.-L. Xiao, S. Paladugu, S. V. Shiyanovskii and O. D. Lavrentovich, *Nat. Commun.*, 2019, **10**, 3749.
42 S. Aya and F. Araoka, *Nat. Commun.*, 2020, **11**, 3248.
43 D. K. Sahu and S. Dhara, *Phys. Rev. Appl.*, 2020, **14**, 034004.
44 J.-Y. Tinevez, N. Perry, J. Schindelin, G. M. Hoopes, G. D. Reynolds, E. Laplantine, S. Y. Bednarek, S. L. Shorte and K. W. Eliceiri, *Methods*, 2017, **115**, 80–90.
45 D. Ershov, M.-S. Phan, J. W. Pylvänäinen, S. U. Rigaud, L. Le Blanc, A. Charles-Orszag, J. R. W. Conway, R. F. Laine, N. H. Roy, D. Bonazzi, G. Duménil, G. Jacquemet and J.-Y. Tinevez, *Nat. Methods*, 2022, **19**, 829–832.
46 J. C. Loudet, P. Hanusse and P. Poulin, *Science*, 2004, **306**, 1525.
47 T. Turiv, I. Lazo, A. Brodin, B. I. Lev, V. Reiffenrath, V. G. Nazarenko and O. D. Lavrentovich, *Science*, 2013, **342**, 1351–1354.
48 I.-S. Baik, J.-H. Choi, B.-S. Jung, S.-Y. Jeon, E.-G. Song and S.-H. Lee, *Trans. Electr. Electron. Mater.*, 2006, **7**, 30–35.
49 F. V. Podgornov, A. V. Ryzhkova and W. Haase, *J. Mol. Liq.*, 2018, **267**, 345–352.
50 Y. Nishioka, F. Kobayashi, N. Sakurai, Y. Sasaki and H. Orihara, *Liq. Cryst.*, 2015, **43**, 427–435.
51 B.-X. Li, R.-L. Xiao, S. V. Shiyanovskii and O. D. Lavrentovich, *Phys. Rev. Res.*, 2020, **2**, 013178.
52 Y. Sasaki, H. Hoshikawa, T. Seto, F. Kobayashi, V. S. R. Jampani, S. Herminghaus, C. Bahr and H. Orihara, *Langmuir*, 2015, **31**, 3815–3819.
53 Y. Sasaki, Y. Takikawa, V. S. R. Jampani, H. Hoshikawa, T. Seto, C. Bahr, S. Herminghaus, Y. Hidaka and H. Orihara, *Soft Matter*, 2014, **10**, 8813–8820.
54 K. Takahashi and Y. Kimura, *Phys. Rev. E: Stat., Nonlinear, Soft Matter Phys.*, 2014, **90**, 012502.
55 O. D. Lavrentovich, *Soft Matter*, 2014, **10**, 1264–1283.
56 M. V. Rasna, U. V. Ramudu, R. Chandrasekar and S. Dhara, *Phys. Rev. E*, 2017, **95**, 012710.